Hyperspectral Super-Resolution Using Nonlinear Unmixing and Nonnegative Tensor Factorization

Qingke Zou, Jie Zhou
College of Mathematics
Sichuan University
Chengdu, Sichuan 610064, China
m18208258544@163.com, jzhou@scu.edu.cn

***Abstract*—Fusing a hyperspectral image (HSI) and a multispectral image (MSI) to generate a super-resolution image (SRI) with refined spatial and spectral resolution is a popular technique in hyperspectral super-resolution (HSR). Most HSR methods accomplish this task by matrix or tensor decomposition in the framework of linear unmixing. Although these methods are effective to some extent, serious challenges remain. In this work, the linear unmixing is extended to nonlinear unmixing framework and a novel HSR method based on a generalized bilinear unmixing model in tensor format is proposed. Apart from the linear part, it additionally considers bilinear interactions between endmembers. A low-rank prior is incorporated into the abundance maps and nonlinear interaction abundance maps, which can adequately model non-local similarities in images. In addition, the total variance is used to explore the local spatial relationships of the image. The optimization is implemented using the alternating direction method of multipliers (ADMM) algorithm with analytical expressions for each iterative update step, which is difficult to implement even for algorithms that focus on nonlinear unmixing. The proposed method overcomes the inherent linear limitations of the linear unmixing framework and avoids the information loss caused by matrixing the HSI and MSI with 3D-structure. The experimental results of simulations on real hyperspectral datasets demonstrate the superiority of the proposed approach over the compared HSR methods.**

***Keywords*—Image fusion, hyperspectral super-resolution, nonlinear unmixing, tensor decomposition, regularization.**

I. Introduction

Hyperspectral image (HSI) contains rich spectral information that facilitates the discrimination of different materials in a scene, and is therefore widely applied in various fields [1]. However, the spatial resolution of HSI is usually low, limited by the trade-off of imaging spectrometer. Such inherent limitation poses a challenge to effectively accomplish various tasks such as vegetation classification and target detection problems. Therefore, improving the spatial resolution of HSI is imminent and has attracted increasing attention. In many situations, it is unfeasible to improve the spatial resolution by upgrading the hardware facilities of the imaging spectrometer, so the use of post-processing techniques to obtain high spatial resolution HSI is favored [2]. On the other hand, a multispectral image (MSI) generated by a multispectral sensor has high spatial resolution but coarse spectral resolution. In order to capture the advantages of both HSI and MSI, a series of hyperspectral super-resolution (HSR) methods have been proposed. The HSR methods aim to fuse information from HSI, which has high spectral resolution but insufficient spatial resolution, and MSI, which exhibits high spatial resolution but coarse spectral resolution, to produce a super-resolution image (SRI) with high spatial and spectral resolution.

The development of HSR technology can be traced back to the 1990s. In the early research, many scholars invested a great deal of effort in fusing hyperspectral and panchromatic images. This technique is known as hyperspectral pansharpening [3]. Existing pansharpening methods are broadly classified into three categories, i.e., multi-resolution analysis [4], [5], component substitution [6], [7], and machine learning [8], [9]. Since it can be viewed as a special case of HSR, the pansharpening method has been widely exploited to address hyperspectral and multispectral image fusion tasks [10], [11]. However, these methods struggle to enhance the spatial resolution of each hyperspectral band due to their rely heavily on spectral resampling techniques [12].

With the rapid development of matrix decomposition and its optimization methods, more and more researches apply them to HSR task. The work on HSR methods based on matrix decomposition stems from the similar idea that HSI and MSI can be decomposed into spectral basis multiplied by some coefficients. Depending on how the spectral basis is modeled, these methods can be divided into two categories: sparse representation and low-rank decomposition. The former treats the spectral basis as an overcomplete dictionary, see, e.g., [13], [14]. The latter assumes that the spectral signal can be represented by a low-dimensional subspace, such as the widely used linear mixture model (LMM) [15], [16]. A common feature of these methods is the processing of the matrixed HSI and MSI, which makes them computationally more affordable.

Despite being computationally simple and to some extent effective, matrix decomposition based methods face some serious drawbacks as well. First, the spectral-spectral and spatial-spectral correlations of HSI and MSI cannot be adequately taken into account at this stage of the process. To address this limitation, several recent studies have employed tensor

This work was supported in part by the Sichuan Science and Technology Program under Grant 2024NSFSC0444, the Key Laboratory of Data Protection and Intelligent Management (Sichuan University), Ministry of Education, China, and also the Fundamental Research Funds for the Central Universities under Grant SCU2023D008.

J. Zhou is the corresponding author.

modeling of the problem. Compared to the HSR methods based on matrix decomposition [17], [18], [19], the methods based on tensor representation naturally treat the HSI or MSI cube as a third-order tensor, which can make full use of its structural information. More importantly, as mentioned in [20], there is no theoretical guarantee for the identifiability of HSR methods based on matrix decomposition. In addition, simple matrix factorization models such as LMM not sufficient to accurately portray real scenes. The LMM is established under the strong assumption that photons interact with only one material before reaching the sensor. Therefore, in order to be more applicable to real scenes, some nonlinear mixing models such as bilinear mixing model (BMM) and high-order mixing model that consider multiple or infinite reflections between photons have been proposed [21], [22], [23], [24], [25].

This work is organized as follows. In Section II, we present the definitions and models required for the later sections. Section III introduces an HSR method utilizing coupled nonnegative tensor decomposition within the framework of nonlinear unmixing. Section IV provides numerical experiments, and Section V gives conclusions.

II. Preliminaries

A. Notations and Definitions

In this subsection, we introduce in detail the notations and definitions used in this work. A scalar, a vector, a matrix, and a tensor are denoted as x, $\mathbf{x}$, $\mathbf{X}$, and $\mathcal{X}$, respectively. $\mathbf{X}_{i,j}$ and $\mathcal{X}_{i,j,k}$ represent (i,j)-th, and (i,j,k)-th element of $\mathbf{X}$ and $\mathcal{X}$ respectively. Some basic operations and definitions about tensor are given as follows.

Definition 1 (Tensor Mode): The dimension of a tensor is named mode. For example, $\mathcal{T} \in \mathbb{R}^{I_1 \times I_2 \times \cdots \times I_N}$ has N modes.

Definition 2 (Slices): A slice is a two-dimensional section of a third-order tensor. The subarrays obtained by fixing one mode are called slices. The horizontal, lateral and frontal slices of the third-order tensor $\mathcal{T}$ are denoted by $\mathcal{T}_{i,:,:}$, $\mathcal{T}_{:,i,:}$ and $\mathcal{T}_{:,:,i}$ respectively.

Definition 3 (Mode-n Product): The mode-n product of a tensor $\mathcal{T} \in \mathbb{R}^{I_1 \times I_2 \times \cdots \times I_n \times \cdots \times I_N}$ with a matrix $\mathbf{X} \in \mathbb{R}^{J_n \times I_n}$ is a tensor $\mathcal{I} \in \mathbb{R}^{I_1 \times I_2 \times \cdots \times I_{n-1} \times J_n \times I_{n+1} \times \cdots \times I_N}$, denoted by

$$\mathcal{I} = \mathcal{T} \times_n \mathbf{X}. \tag{1}$$

From an elemental perspective, we have

$$\mathcal{I}_{i_1,\ldots,i_{n-1},j_n,i_{n+1},\ldots,i_N} = \sum_{i_n=1}^{I_n} \mathcal{T}_{i_1,\ldots,i_N} \mathbf{X}_{j_n,i_n}. \tag{2}$$

B. Nonlinear Spectral Model

The BMM is one of the most popular category of nonlinear mixed models. It extends the LMM by introducing an additional bilinear term to represent second-order interactions between different endmembers. This model overcomes the inherent linear limitations of LMM and captures the main relationships between endmembers. Under the BMM, a pixel $\mathbf{x} \in \mathbb{R}^L$ with L bands can be represented as

$$\mathbf{x} = \mathbf{E}\boldsymbol{\alpha} + \sum_{i=1}^{R-1} \sum_{j=i+1}^{R} \beta_{ij} \mathbf{e}_i \odot \mathbf{e}_j + \mathbf{n}, \tag{3}$$

where, $\mathbf{E} = [\mathbf{e}_1, \ldots, \mathbf{e}_R] \in \mathbb{R}^{L \times R}$, $\boldsymbol{\alpha} = [\alpha_1, \ldots, \alpha_R] \in \mathbb{R}^R$ and $\beta_{ij} \in \mathbb{R}$ denote the matrix consisting of R endmembers, the abundance vector, and the weighting coefficient between the i-th and j-th endmembers, respectively, $\mathbf{n} \in \mathbb{R}^L$ denotes the additive noise, and the symbol $\odot$ represents the Hadamard product [24].

The generalized bilinear model (GBM), as one of the most representative models of BMM, is proposed to meet some physical assumptions. This model will be introduced in the following in terms of both matrix and tensor representations

1) GBM under matrix representation: The GBM is viewed as a generalized form of the LMM, which sets the nonlinear coefficient $\beta_{ij} = \gamma_{ij}\alpha_i\alpha_j$ and satisfies the abundance nonnegativity constraint (ANC) and the abundance sum-to-one constraint (ASC) as follows

$$0 < \gamma_{ij} < 1, \forall\ i < j, \tag{4}$$

$$\gamma_{ij} = 0, \forall\ i \geq j, \tag{5}$$

$$\alpha_i \geq 0, \sum_{i=1}^{R} \alpha_i = 1. \tag{6}$$

Mathematically, the general matrix expression for the BMM of an HSI with N pixels can be written as

$$\mathbf{X} = \mathbf{E}\mathbf{A} + \mathbf{M}\mathbf{B} + \mathbf{N}, \tag{7}$$

where $\mathbf{X} \in \mathbb{R}^{L \times N}$, $\mathbf{A} = [\boldsymbol{\alpha}_1, \ldots, \boldsymbol{\alpha}_N] \in \mathbb{R}^{R \times N}$, $\mathbf{M} = [\mathbf{e}_1 \odot \mathbf{e}_2, \ldots, \mathbf{e}_1 \odot \mathbf{e}_R, \mathbf{e}_2 \odot \mathbf{e}_3, \ldots, \mathbf{e}_{R-1} \odot \mathbf{e}_R] \in \mathbb{R}^{L \times R(R-1)/2}$, $\mathbf{B} \in \mathbb{R}^{R(R-1)/2 \times N}$ and $\mathbf{N} \in \mathbb{R}^{L \times N}$ denote the reshaped SRI matrix, the abundance matrix, the bilinear interaction endmember matrix, the bilinear abundance matrix and the noise matrix, respectively.

2) GBM under tensor representation: The GBM under the matrix representation converts the SRI cube to a matrix, which undoubtedly loses the inherent internal structural information of the SRI. A natural idea is to utilize a tensor representation of the GBM, where the SRI is directly represented by a third-order tensor. Therefore, the cube $\mathcal{X} \in \mathbb{R}^{W \times H \times L}$ can be equivalently expressed in the following form

$$\mathcal{X} = \mathcal{A} \times_3 \mathbf{E} + \mathcal{B} \times_3 \mathbf{M} + \mathcal{N}, \tag{8}$$

where $\mathcal{A} \in \mathbb{R}^{W \times H \times R}$, $\mathcal{B} \in \mathbb{R}^{W \times H \times R(R-1)/2}$ and $\mathcal{N} \in \mathbb{R}^{W \times H \times L}$ denote the abundance cube, bilinear abundance cube and noise cube, respectively.

To facilitate the utilization of the prior structural information on abundance by adding regular terms, we equivalently represent model (8) in the following form

$$\mathcal{X} = \sum_{i=1}^{R} \mathcal{A}_{:,:,i} \circ \mathbf{e}_i + \sum_{j=1}^{R(R-1)/2} \mathcal{B}_{:,:,j} \circ \mathbf{m}_j + \mathcal{N}, \tag{9}$$

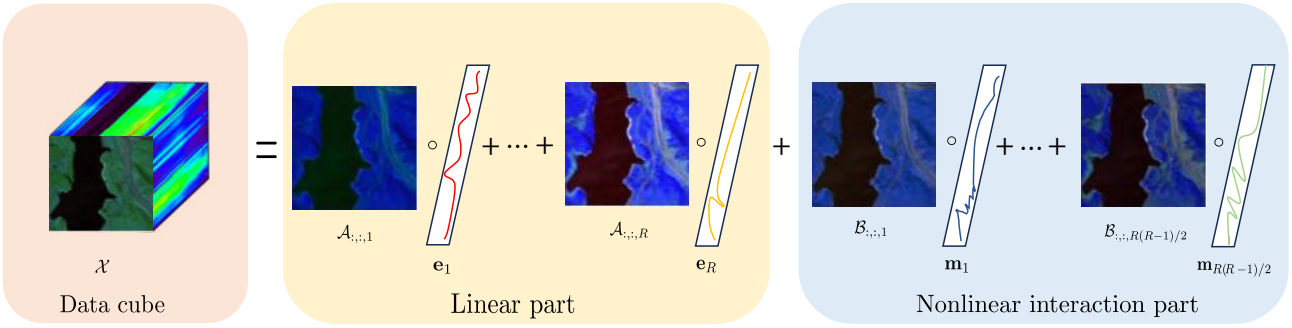

Fig. 1: GBM under tensor representation.

where $\mathcal{A}_{:,:,i} \in \mathbb{R}^{W\times H}$, $\mathcal{B}_{:,:,j} \in \mathbb{R}^{W\times H}$ and $\mathbf{m}_j \in \mathbb{R}^R$ denote the i-th abundance map, the j-th interaction abundance map, and j-th interaction endmember vector, respectively. And the symbol $\circ$ denotes the outer product. As illustrated in Fig. 1, model (9) divides the SRI into a linear part and a nonlinear interaction part, and each factor has a corresponding physical interpretation, i.e., endmember spectral features and abundances. Such a form of decomposition allows us to incorporate prior information into the image processing task to improve performance.

III. Problem Formulation and Method

In order to reconstruct SRI from HSI and MSI, we design an HSR method, named NU-NTF, by combining non-negative tensor decomposition techniques within a nonlinear unmixing framework. In this section, we introduce the proposed method and its optimization in detail.

A. Problem Formulation

Let $\mathcal{X} \in \mathbb{R}^{W\times H\times L}$ denote the SRI with $W \times H$ pixels and L bands. Assume that the HSI and MSI are downsampled/degraded from an SRI, denoted as $\mathcal{Y} \in \mathbb{R}^{w\times h\times L}$ and $\mathcal{Z} \in \mathbb{R}^{W\times H\times l}$ respectively. Note that the SRI has the same spectral resolution as the HSI, the same spatial resolution as the MSI, and typically has $w \le W$, $h \le H$ and $l \le L$.

Assuming the there exist two blurring and downsampling operators, which model the spatial degradation from SRI to HSI, then the HSI observation model can be written as

$$\mathcal{Y} = \mathcal{X} \times_1 \mathbf{D}_w \times_2 \mathbf{D}_h + \mathcal{N}_y, \tag{10}$$

where $\mathbf{D}_w \in \mathbb{R}^{w\times W}$ and $\mathbf{D}_h \in \mathbb{R}^{h\times H}$ contain blurring and downsampling operations for width and height respectively, $\mathcal{N}_y$ is the noise cube.

Further, by considering the spectral degeneracy operator from SRI to MSI, then the observation model of MSI is

$$\mathcal{Z} = \mathcal{X} \times_3 \mathbf{C} + \mathcal{N}_z, \tag{11}$$

where $\mathbf{C}$ models the spectral downsampling and $\mathcal{N}_z$ denotes the observation noise.

Notably, the operators $\mathbf{D}_w$ and $\mathbf{D}_h$ of the spatial degradation are usually modeled as some kernel functions [20], which are considered to be related to the modulation transfer function of the hyperspectral sensor. In addition, the spectral downsampling operator $\mathbf{C}$ can be modeled as a band-selection and averaging matrix, which generally depends on the relative spectral responses of the multispectral sensor [26]. All three operators are assumed to be known.

We wish to fuse HSI and MSI from the observation models (10) and (11). Thus, the HSR problem can be formulated as

$$\min_{\mathcal{X}} \ \frac{1}{2}\|\mathcal{Y} - \mathcal{X} \times_1 \mathbf{D}_w \times_2 \mathbf{D}_h\|_F^2 + \frac{\lambda}{2}\|\mathcal{Z} - \mathcal{X} \times_3 \mathbf{C}\|_F^2, \tag{12}$$

where $\lambda > 0$ is the weight adjustment parameter and $\|\cdot\|_F$ denotes the Frobenius norm which returns the square root of the sum of the squares of all elements.

The use of prior information is often essential to enhance reconstruction performance in noisy environments. Therefore, we adopt the above tensor representation of the GBM model (9) to express the SRI, which facilitates the introduction of additional prior for constraints. The HSR problem is reformulated to solve the following optimization problem

$$\begin{aligned}
\min_{\substack{\mathcal{A}_{:,:,i}\ge 0, \mathcal{B}_{:,:,j}\ge 0\\ \mathbf{e}_i, i=1,\dots,R\\ j=1,\dots,R(R-1)/2}} \ & \frac{1}{2}\left\|\mathcal{Y} - \left(\sum_{i=1}^{R} \mathcal{A}_{:,:,i}\circ\mathbf{e}_i\right)\times_1 \mathbf{D}_w \times_2 \mathbf{D}_h \right.\\
& \left. - \left(\sum_{j=1}^{R(R-1)/2} \mathcal{B}_{:,:,j}\circ\mathbf{m}_j\right)\times_1 \mathbf{D}_w \times_2 \mathbf{D}_h\right\|_F^2\\
& + \frac{\lambda}{2}\left\|\mathcal{Z} - \left(\sum_{i=1}^{R} \mathcal{A}_{:,:,i}\circ\mathbf{e}_i\right)\times_3 \mathbf{C} \right.\\
& \left. - \left(\sum_{j=1}^{R(R-1)/2} \mathcal{B}_{:,:,j}\circ\mathbf{m}_j\right)\times_3 \mathbf{C}\right\|_F^2\\
& + \psi(\mathcal{A}_{:,:,i}) + \varphi(\mathcal{B}_{:,:,j})\\
\text{s.t.} \ & \sum_{i=1}^{R} \mathcal{A}_{:,:,i} = \mathbf{1}_W\mathbf{1}_H^{\mathrm{T}},
\end{aligned} \tag{13}$$

where, $\psi(\mathcal{A}_{:,:,i})$ and $\psi(\mathcal{B}_{:,:,j})$ are regularization terms for abundance maps $\mathcal{A}_{:,:,i}$ and $\mathcal{B}_{:,:,j}$ respectively, and $(\cdot)^{\mathrm{T}}$ means the transpose. The constraint is designed to satisfy the ASC, and $\mathbf{1}_n$ is the $n \times 1$ vector with all entries 1.

Model (13) builds on the nonlinear unmixing of SRI and accomplishes the HSR task by estimating endmembers and abundances. Therefore, it is particularly important to utilize physical prior information to improve the performance of reconstructed SRI. The endmembers are strongly spatially dependent, i.e., a particular endmember tends to be spatially clustered. This characteristic is reflected in the abundance, allowing us to approximate it with a low-rank matrix. Moreover, it is this feature that gives the abundance maps a strong local smooth structure in spatial terms. Inspired by these reasons, we use the nuclear norm to replace the rank constraint and employ the total variation (TV) to explore the local spatial relations of the abundance maps. To be specific, the regularization function of the abundance map is given as

$$\psi(\mathcal{A}_{:,:,i}) = \gamma_1 \sum_{i=1}^{R} \|\mathcal{A}_{:,:,i}\|_* + \beta \sum_{i=1}^{R} \|\mathcal{A}_{:,:,i}\|_{\mathrm{TV}}, \tag{14}$$

where, $\|\mathcal{A}_{:,:,i}\|_* = \sum_{k=1}^{r} \sigma_k(\mathcal{A}_{:,:,i})$ is the nuclear norm with $r = \mathrm{rank}(\mathcal{A}_{:,:,i})$ and $\sigma_k(\mathcal{A}_{:,:,i})$ being the k-th singular value of $\mathcal{A}_{:,:,i}$, $\|\mathcal{A}_{:,:,i}\|_{\mathrm{TV}} = \sum_{j,k} (|a_{j,k} - a_{j-1,k}| + |a_{j,k} - a_{j,k-1}|)$ represents the TV regularization, here $a_{j,k}$ is the (j,k)-th entry of $\mathcal{A}_{:,:,i}$, and $\gamma_1 > 0$ and $\beta > 0$ are regularization parameters.

For the interaction abundance maps, it has been shown that they also have a similar low-rank structure [27]. Therefore, we can use the following regularization function

$$\psi(\mathcal{B}_{:,:,j}) = \gamma_2 \sum_{j=1}^{R(R-1)/2} \|\mathcal{B}_{:,:,j}\|_*, \tag{15}$$

where $\|\mathcal{B}_{:,:,j}\|_*$ denotes the nuclear norm of $\mathcal{B}_{:,:,j}$ and $\gamma_2 > 0$ is the parameter of regularization.

B. Optimization Procedure

The optimization problem (13) can be solved by using alternating direction method of multipliers (ADMM) method. By introducing multiple auxiliary variables $\mathbf{U}_i$, $\mathbf{v}_i$, $\mathbf{H}_i$, $\mathbf{A}_i$, $\mathbf{B}_i$ $(i = 1, \ldots, R)$, $\mathbf{F}_j$, $\mathbf{K}_j$ $(j = 1, \ldots, R(R-1)/2)$, $\mathcal{J}$ and $\mathcal{Q}$, the problem (13) is transformed into the following form

$$\begin{aligned}
\min_{\mathcal{A},\mathcal{B},\mathbf{E}} \ & \frac{1}{2}\left\|\mathcal{Y} - \sum_{i=1}^{R}(\mathbf{U}_i\mathbf{D}_h^{\mathrm{T}}) \circ \mathbf{e}_i - \sum_{j=1}^{R(R-1)/2}(\mathbf{F}_j\mathbf{D}_h^{\mathrm{T}}) \circ \mathbf{m}_j\right\|_F^2 \\
& + \frac{\lambda}{2}\left\|\mathcal{Z} - \sum_{i=1}^{R}\mathcal{A}_{:,:,i} \circ \mathbf{v}_i - \sum_{j=1}^{R(R-1)/2}\mathcal{B}_{:,:,j} \circ \tilde{\mathbf{v}}_j\right\|_F^2 \\
& + \gamma_1\left(\sum_{i=1}^{R}\|\mathbf{H}_i\|_*\right) + \gamma_2\left(\sum_{j=1}^{R(R-1)/2}\|\mathbf{K}_j\|_*\right) \\
& + \beta\|\mathbf{B}_i\|_1 + l_{R^+}(\mathcal{J}) + l_{R^+}(\mathcal{Q}) \\
\text{s.t.} \ & \sum_{i=1}^{R}\mathcal{A}_{:,:,i} = \mathbf{1}_W\mathbf{1}_H^{\mathrm{T}}, \\
& \mathbf{D}_w\mathcal{A}_{:,:,i} = \mathbf{U}_i, i = 1, \ldots, R, \\
& \mathbf{D}_w\mathcal{B}_{:,:,j} = \mathbf{F}_j, j = 1, \ldots, R(R-1)/2, \\
& \mathbf{C}\mathbf{e}_i = \mathbf{v}_i, i = 1, \ldots, R, \\
& \mathcal{A}_{:,:,i} = \mathbf{H}_i, i = 1, \ldots, R, \\
& \mathcal{A}_{:,:,i} = \mathbf{A}_i, i = 1, \ldots, R, \\
& \mathcal{D}(\mathbf{A}_i) = \mathbf{B}_i, i = 1, \ldots, R, \\
& \mathcal{B}_{:,:,j} = \mathbf{K}_j, j = 1, \ldots, R(R-1)/2, \\
& \mathcal{A} = \mathcal{J}, \mathcal{B} = \mathcal{Q},
\end{aligned} \tag{16}$$

where $\tilde{\mathbf{v}}_j$ is the j-th column of matrix $[\mathbf{v}_1 \odot \mathbf{v}_2, \ldots, \mathbf{v}_1 \odot \mathbf{v}_R, \mathbf{v}_2 \odot \mathbf{v}_3, \ldots, \mathbf{v}_{R-1} \odot \mathbf{v}_R]$. $\mathcal{D}(\cdot) = [\mathcal{D}_h(\cdot); \mathcal{D}_v(\cdot)]$ is a difference operator, $\mathcal{D}_h(\cdot)$ and $\mathcal{D}_v(\cdot)$ are used to represent the differentiations in the horizontal and vertical directions, respectively. The operator $l_{R^+}(\cdot)$, for meeting ANC, is defined as

$$l_{R^+}(\mathcal{J}) = \begin{cases} 0, & \mathcal{J} \geq 0, \\ +\infty, & \mathcal{J} < 0. \end{cases} \tag{17}$$

Denote the objective function of the optimization problem in (16) as $\Phi(\mathcal{A}, \mathcal{B}, \mathbf{E})$. The Lagrangian function of optimization problem (16) is given by

$$\begin{aligned}
& \mathcal{L}(\mathcal{A}_{:,:,i}, \mathcal{B}_{:,:,j}, \mathbf{e}_i, \mathbf{U}_i, \mathbf{F}_j, \mathbf{v}_i, \mathbf{H}_i, \mathbf{K}_j, \mathbf{A}_i, \mathbf{B}_i, \mathcal{J}, \mathcal{Q}, \Xi) \\
& = \Phi(\mathcal{A}, \mathcal{B}, \mathbf{E}) + \frac{\mu}{2}\left(\left\|\sum_{i=1}^{R}\mathcal{A}_{:,:,i} - \mathbf{Q} + \mathbf{W}\right\|_F^2\right. \\
& \quad + \sum_{i=1}^{R}\|\mathbf{D}_w\mathcal{A}_{:,:,i} - \mathbf{U}_i + \mathbf{G}_i\|_F^2 + \|\mathcal{B} - \mathcal{Q} + \mathcal{S}\|_F^2 \\
& \quad + \sum_{i=1}^{R}\|\mathbf{C}\mathbf{e}_i - \mathbf{v}_i + \mathbf{z}_i\|_F^2 + \sum_{i=1}^{R}\|\mathcal{A}_{:,:,i} - \mathbf{H}_i + \mathbf{M}_i\|_F^2 \\
& \quad + \sum_{i=1}^{R}\|\mathcal{A}_{:,:,i} - \mathbf{A}_i + \mathbf{J}_i\|_F^2 + \sum_{i=1}^{R}\|\mathcal{D}(\mathbf{A}_i) - \mathbf{B}_i + \mathbf{S}_i\|_F^2 \\
& \quad + \sum_{j=1}^{R(R-1)/2}\|\mathcal{B}_{:,:,j} - \mathbf{K}_j + \mathbf{T}_j\|_F^2 + \|\mathcal{A} - \mathcal{J} + \mathcal{P}\|_F^2 \\
& \quad \left. + \sum_{j=1}^{R(R-1)/2}\|\mathbf{D}_w\mathcal{B}_{:,:,j} - \mathbf{F}_j + \mathbf{P}_j\|_F^2\right),
\end{aligned} \tag{18}$$

where $\Xi = (\mathbf{W}, \mathbf{G}_i, \mathbf{z}_i, \mathbf{M}_i, \mathbf{J}_i, \mathbf{S}_i, \mathbf{T}_j, \mathbf{P}_j, \mathcal{S}, \mathcal{P})$ is the set of all Lagrange multipliers, $\mathbf{Q} = \mathbf{1}_W\mathbf{1}_H^{\mathrm{T}}$, and $\mu > 0$ denotes the Lagrangian penalty parameter. Thus, we can optimize the augmented Lagrangian function (18) for one variable while fixing the other variables. Specifically, the variables involved in (18) can be updated following the steps in Algorithm 1.

We describe in detail some of the notations in Algorithm 1. In Step 2, $\mathcal{T} = \mathcal{Z} - \sum_{j=1, j\neq i}^{R}\mathcal{A}_{:,:,j}^k \circ \mathbf{v}_j^k - \sum_{j=1}^{R(R-1)/2}\mathcal{B}_{:,:,j}^k \circ \tilde{\mathbf{v}}_j^k$, $\bar{\mathbf{A}} = \sum_{j=1, j\neq i}^{R}\mathcal{A}_{:,:,j}^k$ and v_{di} is the d-th component of $\mathbf{v}_i^k$. In Step 3, $\mathcal{D}^*(\cdot)$ denotes the adjoint operator of $\mathcal{D}(\cdot)$, $\mathrm{fftn}(\cdot)$ and $\mathrm{ifftn}(\cdot)$ indicate the fast Fourier transform and its inverse transform, respectively. $|\cdot|^2$ is the element-wise square. In Step 4, $\mathrm{soft}(\cdot)$ represents the soft-thresholding operator [28].

Algorithm 1 NU-NTF Algorithm For HSR.

Input: HSI $\mathcal{Y}$, MSI $\mathcal{Z}$ and degraded matrices $\mathbf{D}_w$, $\mathbf{D}_h$, $\mathbf{C}$.
Output: Abundance cube $\mathcal{A}$, nonlinear interaction abundance cube $\mathcal{B}$ and endmember matrix $\mathbf{E}$ of the reconstructed SRI.

for $k = 1$: MaxIter **do**

$\mathcal{A}_{:,:,i}^{k+1} = \left(\lambda \sum_{d=1}^{l} v_{di}^2 \mathbf{I}_W + 4\mu \mathbf{I}_W + \mu \mathbf{D}_w^{\mathrm{T}} \mathbf{D}_w\right)^{-1} \times \Big(\lambda \sum_{d=1}^{l} \mathcal{T}_{:,:,d} v_{di} + \mu(\mathbf{Q} - \bar{\mathbf{A}} - \mathbf{W}^k + \mathbf{A}_i^k - \mathbf{J}_i^k + \mathbf{D}_w^{\mathrm{T}}(\mathbf{U}_i^k - \mathbf{G}_i^k) + \mathbf{H}_i^k - \mathbf{M}_i^k - \mathcal{P}_{:,:,i}^k + \mathcal{J}_{:,:,i}^k)\Big)$

$\mathbf{A}_i^{k+1} = \mathrm{ifftn}\left(\dfrac{\mathcal{D}^*(\mathbf{B}_i^k - \mathbf{S}_i^k) + \mathcal{A}_{:,:,i}^{k+1} + \mathbf{J}_i^k}{1 + |\mathrm{fftn}(\mathcal{D}_h)|^2 + |\mathrm{fftn}(\mathcal{D}_v)|^2}\right)$

$\mathbf{B}_i^{k+1} = \mathrm{soft}\left(\mathcal{D}(\mathbf{A}_i^{k+1}) + \mathbf{S}_i^k, \beta/\mu\right)$

$\mathcal{B}_{:,:,j}^{k+1} = \left(\lambda \sum_{d=1}^{l} \tilde{v}_{dj}^2 \mathbf{I}_W + 2\mu \mathbf{I}_W + \mu \mathbf{D}_w^{\mathrm{T}} \mathbf{D}_w\right)^{-1} \times \Big(\lambda \sum_{d=1}^{l} \mathcal{E}_{:,:,d} \tilde{v}_{dj} + \mu \mathbf{D}_w^{\mathrm{T}}(\mathbf{F}_j^k - \mathbf{P}_j^k) + \mu(\mathcal{Q}_{:,:,j}^k - \mathcal{S}_{:,:,j}^k + \mathbf{K}_j^k - \mathbf{T}_j^k)\Big)$

$\mathcal{J}_{:,:,i}^{k+1} = \max(\mathcal{A}_{:,:,i}^{k+1} + \mathcal{P}_{:,:,i}^k, \mathbf{0})$

$\mathcal{Q}_{:,:,j}^{k+1} = \max(\mathcal{B}_{:,:,j}^{k+1} + \mathcal{S}_{:,:,j}^k, \mathbf{0})$

$\mathbf{e}_i^{k+1} = \left(\sum_{d=1}^{h} \bar{\mathbf{u}}_d^{\mathrm{T}} \bar{\mathbf{u}}_d \mathbf{I}_N + \Lambda_1 + \mu \mathbf{C}^{\mathrm{T}} \mathbf{C}\right)^{-1} \times \left(\sum_{d=1}^{h} \mathcal{K}_{:,d,:}^{\mathrm{T}} \bar{\mathbf{u}}_d + \Lambda_2 + \mu \mathbf{C}^{\mathrm{T}} \mathbf{v}_i^k - \mu \mathbf{C}^{\mathrm{T}} \mathbf{z}_i^k\right)$

$\mathbf{E} = \max(\mathbf{E}, \mathbf{0})$

$\mathbf{U}_i^{k+1} = \left(\sum_{d=1}^{L} \mathcal{O}_{:,:,d} e_{di} \mathbf{D}_h + \mu(\mathbf{D}_w \mathcal{A}_{:,:,i}^{k+1} + \mathbf{G}_i^k)\right) \times \left(\sum_{d=1}^{L} e_{di}^2 \mathbf{D}_h^{\mathrm{T}} \mathbf{D}_h + \mu \mathbf{I}_H\right)^{-1}$

$\mathbf{F}_j^{k+1} = \left(\sum_{d=1}^{L} \mathcal{U}_{:,:,d} m_{dj} \mathbf{D}_h + \mu(\mathbf{D}_w \mathcal{B}_{:,:,j}^{k+1} + \mathbf{P}_j^k)\right) \times \left(\sum_{d=1}^{L} m_{dj}^2 \mathbf{D}_h^{\mathrm{T}} \mathbf{D}_h + \mu \mathbf{I}_H\right)^{-1}$

$\mathbf{v}_i^{k+1} = \left(\lambda \sum_{l=1}^{h} \bar{\mathbf{a}}_l^{\mathrm{T}} \bar{\mathbf{a}}_l \mathbf{I}_n + \Lambda_3 + \mu \mathbf{I}_n\right)^{-1} \times \left(\lambda \sum_{l=1}^{h} \mathcal{M}_{:,l,:}^{\mathrm{T}} \bar{\mathbf{a}}_l + \Lambda_4 + \mu \mathbf{C} \mathbf{e}_i^{k+1} + \mu \mathbf{z}_i^k\right)$

$\mathbf{H}_i^{k+1} = \mathbf{U} \bar{\mathbf{S}} \mathbf{Z}^{\mathrm{T}}$

$\mathbf{K}_j^{k+1} = \bar{\mathbf{U}} \bar{\mathbf{S}}_k \bar{\mathbf{Z}}^{\mathrm{T}}$

$\mathbf{S}_i^{k+1} = \mathbf{S}_i^k + \mathcal{D}(\mathbf{A}_i^{k+1}) - \mathbf{B}_i^{k+1}$

$\mathbf{J}_i^{k+1} = \mathbf{J}_i^k + \mathcal{A}_{:,:,i}^{k+1} - \mathbf{A}_i^{k+1}$

$\mathcal{P}_{:,:,i}^{k+1} = \mathcal{P}_{:,:,i}^k + \mathcal{A}_{:,:,i}^{k+1} - \mathcal{J}_{:,:,i}^{k+1}$

$\mathcal{S}_{:,:,j}^{k+1} = \mathcal{S}_{:,:,j}^k + \mathcal{B}_{:,:,j}^{k+1} - \mathcal{Q}_{:,:,j}^{k+1}$

$\mathbf{W}^{k+1} = \mathbf{W}^k + \sum_{i=1}^{R} \mathcal{A}_{:,:,i}^{k+1} - \mathbf{Q}$

$\mathbf{G}_i^{k+1} = \mathbf{G}_i^k + \mathbf{D}_w \mathcal{A}_{:,:,i}^{k+1} - \mathbf{U}_i^{k+1}$

$\mathbf{P}_j^{k+1} = \mathbf{P}_j^k + \mathbf{D}_w \mathcal{B}_{:,:,j}^{k+1} - \mathbf{F}_j^{k+1}$

$\mathbf{z}_i^{k+1} = \mathbf{z}_i^k + \mathbf{C}\mathbf{e}_i^{k+1} - \mathbf{v}_i^{k+1}$

$\mathbf{M}_i^{k+1} = \mathbf{M}_i^k + \mathcal{A}_{:,:,i}^{k+1} - \mathbf{H}_i^{k+1}$

$\mathbf{T}_j^{k+1} = \mathbf{T}_j^k + \mathcal{B}_{:,:,j}^{k+1} - \mathbf{K}_j^{k+1}$

$k = k + 1$

end

In Step 5, $\mathcal{E} = \mathcal{Z} - \sum_{i=1}^{R} \mathcal{A}_{:,:,i}^k \circ \mathbf{v}_i^k - \sum_{k=1,,k\neq j}^{R(R-1)/2} \mathcal{B}_{:,:,j}^k \circ \tilde{\mathbf{v}}_j^k$ and $\tilde{v}_{di}$ is the d-th component of $\tilde{\mathbf{v}}_i^k$. In Step 8,

$$\Lambda_1 = \sum_{d=1}^{h} \sum_{j'=1}^{R-1} \left(\bar{\mathbf{f}}_{dj'}^k\right)^{\mathrm{T}} \bar{\mathbf{f}}_{dj'}^k \left(\mathrm{Diag}(\mathbf{e}_{j'}^k)\right)^2, \tag{19}$$

$$\Lambda_2 = \sum_{d=1}^{h} \sum_{j'=1}^{R-1} \mathrm{Diag}\left(\mathbf{e}_{j'}^k\right) \mathcal{K}_{:,d,:}^{\mathrm{T}} \bar{\mathbf{f}}_{dj'}^k, \tag{20}$$

where, $\bar{\mathbf{u}}_d$ and $\bar{\mathbf{f}}_{dj'}$ are the d-th column of matrix $\mathbf{U}_d^k \mathbf{D}_h^{\mathrm{T}}$ and $\mathbf{F}_{j'}^k \mathbf{D}_h^{\mathrm{T}}$ respectively, j' denotes the $R-1$ subscript indexes except for i, $\mathcal{K} = \mathcal{Y} - \sum_{j=1,j\neq i}^{R} (\mathbf{U}_j^k \mathbf{D}_h^{\mathrm{T}}) \circ \mathbf{e}_j^k - \sum_{\neg j'=1}^{(R-2)(R-1)/2} (\mathbf{F}_{\neg j'}^k \mathbf{D}_h^{\mathrm{T}}) \circ \mathbf{m}_{\neg j'}^k$, and $\neg j'$ denotes $R-2$ subscripts apart from j'. In Step 10, $\mathcal{O} = \mathcal{Y} - \sum_{j=1,j\neq i}^{R} (\mathbf{U}_j^k \mathbf{D}_h^{\mathrm{T}}) \circ \mathbf{e}_j^{k+1} - \sum_{j=1}^{R(R-1)/2} (\mathbf{F}_j \mathbf{D}_h^{\mathrm{T}}) \circ \mathbf{m}_j$. In Step 11, $\mathcal{U} = \mathcal{Y} - \sum_{i=1}^{R} (\mathbf{U}_i^k \mathbf{D}_h^{\mathrm{T}}) \circ \mathbf{e}_i^{k+1} - \sum_{k=1,k\neq j}^{R(R-1)/2} (\mathbf{F}_k \mathbf{D}_h^{\mathrm{T}}) \circ \mathbf{m}_k$. In Step 12,

$$\Lambda_3 = \lambda \sum_{l=1}^{h} \sum_{j'=1}^{R-1} \left(\bar{\mathbf{b}}_{lj'}^k\right)^{\mathrm{T}} \bar{\mathbf{b}}_{lj'}^k \left(\mathrm{Diag}(\mathbf{v}_{j'}^k)\right)^2, \tag{21}$$

$$\Lambda_4 = \lambda \sum_{l=1}^{h} \sum_{j'=1}^{R-1} \mathrm{Diag}\left(\mathbf{v}_{j'}^k\right) \mathcal{M}_{:,l,:}^{\mathrm{T}} \bar{\mathbf{b}}_{lj'}^k, \tag{22}$$

where, $\mathbf{a}_l$ and $\bar{\mathbf{b}}_{lj'}$ are the l-th column of matrix $\mathcal{A}_{:,:,i}^{k+1}$ and $\mathcal{B}_{:,:,j}^{k+1}$ respectively, $\mathcal{M} = \mathcal{Z} - \sum_{j=1,j\neq i}^{R} \mathcal{A}_{:,:,i} \circ \mathbf{v}_i - \sum_{\neg j'=1}^{(R-2)(R-1)/2} \mathcal{B}_{:,:,\neg j'} \circ \tilde{\mathbf{v}}_{\neg j'}$, $\mathrm{Diag}(\cdot)$ returns the column vector consisting of the main diagonal elements if the input variable is a matrix and returns a square matrix with the elements of the vector on the main diagonal if the input variable is a vector. In Step 13, $[\mathbf{U}, \mathbf{S}, \mathbf{Z}] = \mathrm{SVD}(\bar{\mathbf{H}}_i)$ with $\bar{\mathbf{H}}_i = \mathcal{A}_{:,:,i}^{k+1} + \mathbf{M}_i^k$, $\mathrm{SVD}(\cdot)$ represents the singular value decomposition and $\bar{\mathbf{S}} = \mathrm{Diag}\left(\max\left(\mathrm{Diag}(\mathbf{S}) - \gamma_1/\mu, 0\right)\right)$. In Step 14, $[\bar{\mathbf{U}}, \mathbf{S}_k, \bar{\mathbf{Z}}] = \mathrm{SVD}(\bar{\mathbf{K}}_j)$ with $\bar{\mathbf{K}}_j = \mathcal{B}_{:,:,j}^{k+1} + \mathbf{T}_j^k$, and $\bar{\mathbf{S}}_k = \mathrm{Diag}\left(\max\left(\mathrm{Diag}(\mathbf{S}_k) - \gamma_2/\mu, 0\right)\right)$.

IV. Experiments

In this section, we will demonstrate the performance of the proposed method through numerical experiments. All experiments are implemented in Octave on a computer with AMD Ryzen 7 5800H 3.2Ghz processor.

A. Experimental Settings

To evaluate the performance of the proposed NU-NTF method, five classical HSR methods, CNMF [17], HySure [18], FUSE [19], STEREO [20] and SCLL1 [29] are used for comparison. Among these five methods, CNMF, HySure and SCLL1 are linear unmixing based HSR methods. The proposed method uses sunsal [28] and sisal [30] to initialize the endmembers matrix $\mathbf{E}$ and the abundance cube $\mathcal{A}$, respectively. All Lagrange multipliers are initialized with the zero matrix.

1) Evaluation: To assess the reconstruction quality of SRI, we use several of the intuitive metrics introduced in [12] and [3]. Specifically, we adopt the reconstruction signal-to-noise ratio (R-SNR), cross correlation (CC), universal image quality index (UIQI), structural similarity index (SSIM), relative dimensional global error (ERGAS), spectral angle mapper (SAM) and root mean square error (RMSE), whose detailed definitions are given in [3] and [31]. Higher values of R-SNR, CC, UIQI and SSIM, as well as lower values of ERGAS, SAM and RMSE, imply a superior reconstruction accuracy.

2) Degradation Modeling: We complete the semi-real data experiments under the assumption that the operators $\mathbf{D}_w$, $\mathbf{D}_h$ and $\mathbf{C}$, which degenerate from SRI to HSI and MSI, are known. To evaluate the performance of the HSR algorithms, a real hyperspectral image is treated as the SRI, i.e., the 'ground-truth' SRI is known. We follow Wald's protocol as usual to generate the simulated HSI and MSI [32]. In particular, the degradation process from SRI to HSI is modeled as the simultaneous blurring of SRI using a 9×9 Gaussian kernel and downsampling at 4-pixel intervals along two spatial directions. To simulate the acquisition of MSI from SRI, we construct the spectral response matrix $\mathbf{C}$, based on the spectral specifications of the widely adopted multispectral sensors LANDSAT or QuickBird, whose parameter specifications can be found from the websites at 'https://landsat.gsfc.nasa.gov' and 'https://www.satimagingcorp.com/satellite-sensors/quickbird', respectively. In this way, the simulated MSI is obtained by band selection and averaging the SRI over the response matrix $\mathbf{C}$ [20]. In addition, to simulate the real scene, the HSI and MSI are also added with zero-mean white Gaussian noise with different signal-to-noise ratios (SNRs). All experimental results are averaged over 20 Monte-Carlo trials.

B. Semi-Real Data Experiments

In this subsection, two real image datasets (Pavia University and Salinas datasets), are used to evaluate the reconstruction performance of the proposed algorithm.

1) Salinas Dataset: This dataset is taken from Salinas Valley and captured by the 224-band airborne visible/infrared imaging spectrometer. The raw data excluded 20 absorbing bands (108–112, 154–167, and 224), leaving 204 bands available for analysis. It derives from an image with approximately 3.7m spatial resolution, encompassing 512×217 pixels. For this experiment, a subimage with a region size of 80×84 is selected, i.e. $\mathcal{X} \in \mathbb{R}^{80\times84\times204}$. Then, $\mathcal{Y} \in \mathbb{R}^{80\times84\times6}$ and $\mathcal{Z} \in \mathbb{R}^{20\times21\times204}$ are generated by previously described spatial degradation techniques and the LANDSAT spectral degradation, respectively. In this experiment, the proposed method sets the number of endmembers to 4 due to the small selection of subregions, while the compared linear unmixing-based methods select the optimal one between 4 and 9 as the number of endmembers.

Tables I–III show the performance of the algorithms for SNRs in the range of 10–20 dB (hereinafter, the maximum on each row is bolded and the values in parentheses represent the performance under ideal conditions, where time is measured in seconds.). It is clear that NU-NTF significantly outperforms the benchmark methods when the SNR is relatively low. However, the price paid is that it is more time-consuming. This suggests that the algorithm can improve the reconstruction accuracy of SRI by capturing the detailed features of the image in a nonlinear unmixing framework. Unfortunately, it is the presence of its nonlinearity that causes the algorithm to be relatively computationally cumbersome. For larger SNR, e.g., SNR = 20 dB, the performance of NU-NTF is slightly inferior to the SCLL1 method in some metrics, but still outstanding compared to other methods.

TABLE I: Performance for Salinas Data. SNR = 10 dB

Performance	Algorithm					
	CNMF	HySure	FUSE	STEREO	SCLL1	NU-NTF
R-SNR(∞)	14.0300	19.4600	16.3400	18.4800	21.2600	**23.1000**
CC(1)	0.4619	0.7592	0.5730	0.6933	0.8538	**0.9083**
UIQI(1)	0.1246	0.3673	0.1907	0.2204	0.3604	**0.4770**
SSIM(1)	0.5620	0.9115	0.7275	0.7983	0.8890	**0.9460**
ERGAS(0)	6.1220	1.3640	5.0270	2.8950	0.9138	**0.9122**
SAM(0)	0.1430	0.0667	0.1300	0.0905	0.0563	**0.0484**
RMSE(0)	0.0397	0.0213	0.0305	0.0238	0.0173	**0.0140**
Time(0)	1.8740	10.0700	**0.0676**	0.2462	6.4280	90.4300

TABLE II: Performance for Salinas Data. SNR = 15 dB

Performance	Algorithm					
	CNMF	HySure	FUSE	STEREO	SCLL1	NU-NTF
R-SNR(∞)	19.1800	20.3300	18.8200	21.5100	24.2500	**24.5900**
CC(1)	0.7089	0.8270	0.7012	0.8105	0.9130	**0.9291**
UIQI(1)	0.2789	0.4412	0.2989	0.3437	0.5036	**0.5542**
SSIM(1)	0.7829	0.9416	0.8692	0.8940	0.9483	**0.9523**
ERGAS(0)	3.2170	0.8582	2.6300	1.6160	0.7699	**0.5741**
SAM(0)	0.0815	0.0618	0.0824	0.0604	0.0417	**0.0428**
RMSE(0)	0.0229	0.0192	0.0229	0.0168	0.0123	**0.0118**
Time(0)	1.9630	10.2400	**0.0638**	0.2690	7.3110	164.0700

TABLE III: Performance for Salinas Data. SNR = 20 dB

Performance	Algorithm					
	CNMF	HySure	FUSE	STEREO	SCLL1	NU-NTF
R-SNR(∞)	23.6000	21.4700	19.9500	24.2500	**27.0200**	26.1900
CC(1)	0.8836	0.8633	0.8046	0.8429	0.9397	**0.9450**
UIQI(1)	0.5031	0.5355	0.4134	0.4420	0.6151	**0.6189**
SSIM(1)	0.9157	0.9392	0.9317	0.9214	0.9566	**0.9668**
ERGAS(0)	1.6210	0.7296	1.4860	1.5730	**0.4183**	0.4728
SAM(0)	0.0458	0.0539	0.0581	0.0495	**0.0304**	0.0369
RMSE(0)	0.0132	0.0169	0.0201	0.0123	**0.0089**	0.0098
Time(0)	2.2710	10.2500	**0.0676**	0.3699	16.8500	226.7000

Fig. 2 shows the performance of the methods in reconstructing the SRI for the case of SNR = 15 dB, which includes the reconstruction results for the 35-th band, the corresponding residual images (i.e., $|\mathcal{X}_{:,:,k} - \hat{\mathcal{X}}_{:,:,k}|$, $k = 35$), and the SAM maps. As we can see, the reconstructed image by the NU-NTF is indeed visually closer to the ground-truth SRI, and its residual map is all smoother than those of the other algorithms in this band. Moreover, for the SAM maps, the proposed method is relatively more prominent in its ability to capture detailed features.

2) Pavia University Dataset: Another real dataset is collected by the ROSIS sensor over Pavia University, Italy [33].

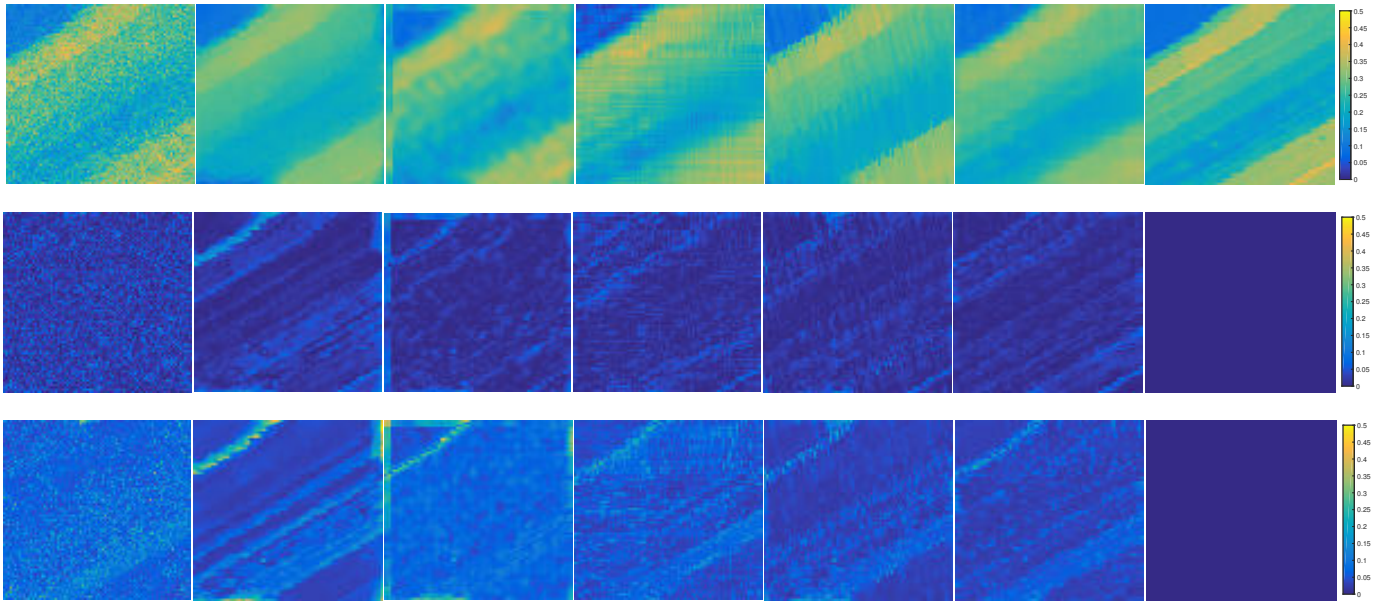

Fig. 2: SRIs reconstruction for Salinas, the corresponding residual images, and the SAM maps. First row: the reconstructed SRIs for the 35-th band; Second row: the residual images for the 35-th band; Third row: the SAM maps.

TABLE IV: Performance on Pavia University Data. SNR = 10 dB

Performance	Algorithm					
	CNMF	HySure	FUSE	STEREO	SCLL1	NU-NTF
R-SNR(∞)	7.6760	10.8600	13.2700	14.0800	13.5400	**14.6000**
CC(1)	0.7454	0.8396	0.8657	0.9007	0.8885	**0.9182**
UIQI(1)	0.4047	0.5125	0.5339	0.6151	0.6218	**0.6764**
SSIM(1)	0.4147	0.5310	0.6741	0.6643	0.6625	**0.7864**
ERGAS(0)	1.9900	1.4440	1.1630	1.0210	1.0780	**0.9510**
SAM(0)	0.3871	0.2542	0.1610	0.1716	0.1653	**0.1265**
RMSE(0)	0.0855	0.0593	0.0449	0.0409	0.0435	**0.0385**
Time(0)	44.2700	267.4800	**0.8516**	7.4010	399.5800	457.5100

TABLE V: Performance on Pavia University Data. SNR = 15 dB

Performance	Algorithm					
	CNMF	HySure	FUSE	STEREO	SCLL1	NU-NTF
R-SNR(∞)	12.6900	17.6300	14.1200	17.1800	17.8400	**18.1900**
CC(1)	0.8855	0.9541	0.8945	0.9485	0.9552	**0.9588**
UIQI(1)	0.6005	0.7890	0.6096	0.7396	0.7502	**0.7808**
SSIM(1)	0.6331	0.8726	0.7367	0.8007	0.8090	**0.8446**
ERGAS(0)	1.1900	0.6804	1.0370	0.7283	0.6814	**0.6620**
SAM(0)	0.2252	0.1123	0.1221	0.1261	0.1155	**0.1086**
RMSE(0)	0.0480	0.0272	0.0408	0.0286	0.0296	**0.0255**
Time(0)	43.8200	260.5300	**0.8492**	12.8400	404.3800	465.3200

The entire image comprises 608×336 pixels with 103 spectral bands. The sizes of HSI and MSI are $608 \times 336 \times 4$ and $152 \times 84 \times 103$, respectively, and the latter is generated using QuickBird spectral degradation specification. The number of endmembers is set similarly to the Salinas dataset experiments.

Tables IV and V show that the NU-NTF generates the best reconstruction accuracy under different SNRs. Close behind are SCLL1 and STEREO, which also show good performance, and both are tensor decomposition based HSR methods. In terms of runtime performance, the proposed methods consume a significant amount of computational cost. In contrast, the FUSE is the most efficient algorithm, but its reconstruction accuracy is severely affected by model mismatch.

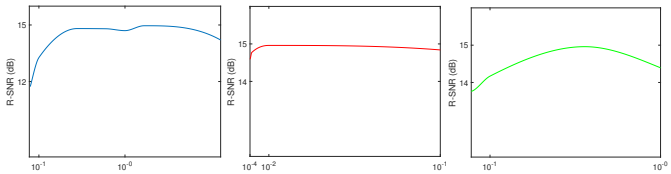

(a) μ (b) β (c) γ_1

Fig. 3: The R-SNR (dB) reconstructed HSI under different μ, β and γ_1 on the Salinas data.

3) Parameter Selection: In the proposed NU-NTF algorithm, we set $\lambda = 1$ and $\gamma_1 = \gamma_2$. For the regularization parameters μ, β and γ_1, we reconstruct the HSI (or MSI) based on the degenerate operations $\mathbf{C}$ (or $\mathbf{D}_w$ and $\mathbf{D}_h$) and the SRI generated by the HSR algorithm, which is then adjusted by the reconstruction accuracy of the HSI (or MSI). As an example, for the experiments on the Salinas dataset under SNR = 15 dB, the iteration is terminated when the relative error of reconstruction between two consecutive iterations of NU-NTF is less than 10^{-4} or the number of iterations exceeds 425.

Fig. 3 demonstrates the R-SNR of the reconstructed HSI for different parameters at SNR = 15 dB. Note that when one parameter is considered, the other parameters will be fixed to the "optimal value". It can be observed that the value of the parameter β has a slight effect on the reconstruction accuracy within a certain range. Comparatively, the variation of the other two parameters causes large fluctuations in the performance.

V. Conclusion

In this work, an NU-NTF method has been proposed to tackle the HSR problem. Under the framework of nonlinear unmixing, the SRI is reconstructed by employing a nonnegative tensor decomposition to estimate the potential factors endmembers and abundance maps. The proposed algorithm breaks through the inherent limitations of the linear unmixing-based HSR method and has analytical expressions at the iterations for optimally solving the HSR problem by employing the ADMM method. Simulated comparison experiments for some real HSI datasets demonstrate that the NU-NTF performs well in the vast majority of cases. The adoption of nonlinear unmixing technique for significantly improving the HSR performance also increases computational cost. The future research will devote to the reduction of computational complexity.

References

[1] H. F. Grahn and P. Geladi, Eds., *Techniques and Applications of Hyperspectral Image Analysis*. Chichester, UK: John Wiley & Sons, 2007.

[2] T. Akgun, Y. Altunbasak, and R. Mersereau, "Super-resolution reconstruction of hyperspectral images," *IEEE Transactions on Image Processing*, vol. 14, no. 11, pp. 1860–1875, Nov. 2005.

[3] L. Loncan, L. B. de Almeida, J. M. Bioucas-Dias, X. Briottet, J. Chanussot, N. Dobigeon, S. Fabre, W. Liao, G. A. Licciardi, M. Simoes, J.-Y. Tourneret, M. A. Veganzones, G. Vivone, Q. Wei, and N. Yokoya, "Hyperspectral pansharpening: A review," *IEEE Geoscience and Remote Sensing Magazine*, vol. 3, no. 3, pp. 27–46, Sep. 2015.

[4] G. Vivone, R. Restaino, and J. Chanussot, "Full scale regression-based injection coefficients for panchromatic sharpening," *IEEE Transactions on Image Processing*, vol. 27, no. 7, pp. 3418–3431, Jul. 2018.

[5] G. Vivone, S. Marano, and J. Chanussot, "Pansharpening: Context-based generalized laplacian pyramids by robust regression," *IEEE Transactions on Geoscience and Remote Sensing*, vol. 58, no. 9, pp. 6152–6167, Sep. 2020.

[6] R. Restaino, M. Dalla Mura, G. Vivone, and J. Chanussot, "Context-adaptive pansharpening based on image segmentation," *IEEE Transactions on Geoscience and Remote Sensing*, vol. 55, no. 2, pp. 753–766, Feb. 2017.

[7] G. Vivone, "Robust band-dependent spatial-detail approaches for panchromatic sharpening," *IEEE Transactions on Geoscience and Remote Sensing*, vol. 57, no. 9, pp. 6421–6433, Sep. 2019.

[8] G. Masi, D. Cozzolino, L. Verdoliva, and G. Scarpa, "Pansharpening by convolutional neural networks," *Remote Sensing*, vol. 8, no. 7, pp. 1–22, Jul. 2016, Art. no. 594.

[9] L.-J. Deng, G. Vivone, C. Jin, and J. Chanussot, "Detail injection-based deep convolutional neural networks for pansharpening," *IEEE Transactions on Geoscience and Remote Sensing*, vol. 59, no. 8, pp. 6995–7010, Aug. 2021.

[10] Z. Chen, H. Pu, B. Wang, and G.-M. Jiang, "Fusion of hyperspectral and multispectral images: A novel framework based on generalization of pan-sharpening methods," *IEEE Geoscience and Remote Sensing Letters*, vol. 11, no. 8, pp. 1418–1422, Aug. 2014.

[11] M. Selva, B. Aiazzi, F. Butera, L. Chiarantini, and S. Baronti, "Hyper-sharpening: A first approach on SIM-GA data," *IEEE Journal of Selected Topics in Applied Earth Observations and Remote Sensing*, vol. 8, no. 6, pp. 3008–3024, Jun. 2015.

[12] N. Yokoya, C. Grohnfeldt, and J. Chanussot, "Hyperspectral and multispectral data fusion: A comparative review of the recent literature," *IEEE Geoscience and Remote Sensing Magazine*, vol. 5, no. 2, pp. 29–56, Jun. 2017.

[13] R. Kawakami, Y. Matsushita, J. Wright, M. Ben-Ezra, Y.-W. Tai, and K. Ikeuchi, "High-resolution hyperspectral imaging via matrix factorization," in *IEEE Conference on Computer Vision and Pattern Recognition*, Colorado Springs, CO, USA, Jun. 2011, pp. 2329–2336.

[14] Q. Wei, J. Bioucas-Dias, N. Dobigeon, and J.-Y. Tourneret, "Hyperspectral and multispectral image fusion based on a sparse representation," *IEEE Transactions on Geoscience and Remote Sensing*, vol. 53, no. 7, pp. 3658–3668, Jul. 2015.

[15] Q. Li, W.-K. Ma, and Q. Wu, "Hyperspectral super-resolution: Exact recovery in polynomial time," in *2018 IEEE Statistical Signal Processing Workshop*, Freiburg im Breisgau, Germany, Jun. 2018, pp. 378–382.

[16] H. Liu, R. Wu, and W.-K. Ma, "Is there any recovery guarantee with coupled structured matrix factorization for hyperspectral super-resolution?" in *2019 IEEE 8th International Workshop on Computational Advances in Multi-Sensor Adaptive Processing*, Le Gosier, Guadeloupe, Dec. 2019, pp. 480–484.

[17] N. Yokoya, T. Yairi, and A. Iwasaki, "Coupled nonnegative matrix factorization unmixing for hyperspectral and multispectral data fusion," *IEEE Transactions on Geoscience and Remote Sensing*, vol. 50, no. 2, pp. 528–537, Feb. 2012.

[18] M. Simoes, J. Bioucas-Dias, L. B. Almeida, and J. Chanussot, "A convex formulation for hyperspectral image superresolution via subspace-based regularization," *IEEE Transactions on Geoscience and Remote Sensing*, vol. 53, no. 6, pp. 3373–3388, Jun. 2015.

[19] Q. Wei, N. Dobigeon, and J.-Y. Tourneret, "Fast fusion of multi-band images based on solving a sylvester equation," *IEEE Transactions on Image Processing*, vol. 24, no. 11, pp. 4109–4121, Nov. 2015.

[20] C. I. Kanatsoulis, X. Fu, N. D. Sidiropoulos, and W.-K. Ma, "Hyperspectral super-resolution: A coupled tensor factorization approach," *IEEE Transactions on Signal Processing*, vol. 66, no. 24, pp. 6503–6517, Dec. 2018.

[21] W. Fan, B. Hu, J. Miller, and M. Li, "Comparative study between a new nonlinear model and common linear model for analysing laboratory simulated-forest hyperspectral data," *International Journal of Remote Sensing*, vol. 30, no. 11, pp. 2951–2962, Jun. 2009.

[22] A. Halimi, Y. Altmann, N. Dobigeon, and J.-Y. Tourneret, "Nonlinear unmixing of hyperspectral images using a generalized bilinear model," in *2011 IEEE Statistical Signal Processing Workshop*, Nice, France, Jun. 2011, pp. 413–416.

[23] I. Meganem, P. Deliot, X. Briottet, Y. Deville, and S. Hosseini, "Linear–quadratic mixing model for reflectances in urban environments," *IEEE Transactions on Geoscience and Remote Sensing*, vol. 52, no. 1, pp. 544–558, Jan. 2014.

[24] R. Heylen and P. Scheunders, "A multilinear mixing model for nonlinear spectral unmixing," *IEEE Transactions on Geoscience and Remote Sensing*, vol. 54, no. 1, pp. 240–251, Jan. 2016.

[25] M. Tang, B. Zhang, A. Marinoni, L. Gao, and P. Gamba, "Multiharmonic postnonlinear mixing model for hyperspectral nonlinear unmixing," *IEEE Geoscience and Remote Sensing Letters*, vol. 15, no. 11, pp. 1765–1769, Nov. 2018.

[26] G. Vivone, "Multispectral and hyperspectral image fusion in remote sensing: A survey," *Information Fusion*, vol. 89, pp. 405–417, Jan. 2023.

[27] L. Gao, Z. Wang, L. Zhuang, H. Yu, B. Zhang, and J. Chanussot, "Using low-rank representation of abundance maps and nonnegative tensor factorization for hyperspectral nonlinear unmixing," *IEEE Transactions on Geoscience and Remote Sensing*, vol. 60, pp. 1–17, 2022.

[28] J. M. Bioucas-Dias and M. A. T. Figueiredo, "Alternating direction algorithms for constrained sparse regression: Application to hyperspectral unmixing," in *2010 2nd Workshop on Hyperspectral Image and Signal Processing: Evolution in Remote Sensing*, Reykjavik, Iceland, Jun. 2010, pp. 1–4.

[29] M. Ding, X. Fu, T.-Z. Huang, J. Wang, and X.-L. Zhao, "Hyperspectral super-resolution via interpretable block-term tensor modeling," *IEEE Journal of Selected Topics in Signal Processing*, vol. 15, no. 3, pp. 641–656, Apr. 2021.

[30] J. Bioucas-Dias, "A variable splitting augmented Lagrangian approach to linear spectral unmixing," in *2009 First Workshop on Hyperspectral Image and Signal Processing: Evolution in Remote Sensing*, Grenoble, France, Aug. 2009, pp. 1–4.

[31] Q. Wei, J. Bioucas-Dias, N. Dobigeon, J.-Y. Tourneret, M. Chen, and S. Godsill, "Multiband image fusion based on spectral unmixing," *IEEE Transactions on Geoscience and Remote Sensing*, vol. 54, no. 12, pp. 7236–7249, Dec. 2016.

[32] Y. Zeng, W. Huang, M. Liu, H. Zhang, and B. Zou, "Fusion of satellite images in urban area: Assessing the quality of resulting images," in *2010 18th IEEE International Conference on Geoinformatics*, Beijing, China, Jun. 2010, pp. 1–4.

[33] B. Kunkel, F. Blechinger, R. Lutz, R. Doerffer, H. van der Piepen, and M. Schroder, "ROSIS (reflective optics system imaging spectrometer) - A candidate instrument for polar platform missions," in *Proceedings of the SPIE: Optoelectronic Technologies for Remote Sensing from Space*, vol. 868, Cannes, France, Apr. 1988, pp. 131–141.